Computer Physics Communications 182 (2011) 289–298

Contents lists available at ScienceDirect

Computer Physics Communications

www.elsevier.com/locate/cpc

Application of coordinate transformation and finite differences method in numerical modeling of quantum dash band structure

B.M. Stupovski, J.V. Crnjanski, D.M. Gvozdić *

School of Electrical Engineering, University of Belgrade, Bulevar Kralja Aleksandra 73b, P.O. Box 35-54, 11120 Belgrade, Serbia

ARTICLE INFO

Article history:
Received 22 March 2010
Received in revised form 17 September 2010
Accepted 21 September 2010
Available online 25 September 2010

Keywords:
Quantum dashes
Electronic band structure
Coordinate transformation
Finite difference

ABSTRACT

In this paper we propose an efficient and simple method for the band structure calculation of semiconductor quantum dashes. The method combines a coordinate transformation (mapping) based on an analytical function and the finite differences method (FDM) for solving the single-band Schrödinger equation. We explore suitable coordinate transformations and propose those, which might simultaneously provide a satisfactory fit of the quantum dash heterointerface and creation of an appropriate computational domain which encloses the quantum dash structure. After mapping of the quantum dash and the rest of computational domain, the Schrödinger equation is solved by the FDM in the mapped space. For the proposed coordinate transformations, we investigate and analyze applicability, robustness and convergence of the method by varying the FDM grid density and size of the computational domain. We find that the method provides sufficient accuracy, stability and flexibility with respect to the size and shape of the quantum dash and above all, extreme simplicity, which is promising and essential for an extension of the method to the multiband Schrödinger equation case.

1. Introduction

Presently, there is a strong interest in self-assembled semiconductor quantum nanostructures due to their new and advanced electronic and optical properties. From the technological point of view, their significant advantage is self-assembling process of growth, which doesn't require any additional lithographic steps. The most interesting applications of these structures are usually related to semiconductor lasers and optical amplifiers [1–5], where self-assembled quantum nanostructures are used as an active region, providing for low threshold current [6], low chirp and small linewidth enhancement factor [7].

One of the most recent and intriguing representatives of the self-assembled quantum nanostructures are quantum dashes (QDHs), which are wire-like semiconductor nanostructures. The self-assembling growth process leads to an ensemble of QDHs with significant size fluctuation with respect to their widths, heights and lengths [8–10]. The size fluctuation considerably affects the QDHs band structure and consequently electronic and optical characteristics [2,8,11,12]. In order to theoretically analyze an ensemble of QDHs it is important to develop an efficient, accurate and simple method for the band structure calculation, which can handle arbitrary profile of a single QDH.

Although there is a group of methods (e.g. empirical pseudopotential method, tight-binding method [13,14], etc.) which can be used for calculation of the QDH band structure by including the potentials of individual atoms, these methods are computationally very demanding. The more efficient method, which has been widely used during several decades, is the envelope function approximation (EFA). An essential assumption in the derivation of the EFA is that potential is slowly varying on the scale of the lattice constant. The advantage and numerical efficiency of the EFA come from the fact that one can avoid the explicit inclusion of the cell periodic potential and that only the slowly varying perturbation enters the Hamiltonian. In this case, the Schrödinger equation involves the slowly varying part of the wavefunction.

The most commonly used numerical method for implementation of the EFA in calculation of the band structure for one- and zero-dimensional irregular nanostructures is the finite element method (FEM) [15–17]. This method provides high flexibility and it can be implemented even when heterointerfaces are such that it is difficult to describe them by analytical functions. Since basis functions in the FEM are relatively simple, the discretization matrix can be easily set and efficiently evaluated. Although, in this case, the discretization matrix is sparse, its size is usually very large, depending on the computational domain size and the mesh density. However, the major drawback of the FEM is that in addition it requires specialized routines for automatic or manual mesh generation. The mesh itself, if not carefully generated, can affect the accuracy of the calculation and lead to unnecessarily large discretization matrices and eigenvalue problems.

* Corresponding author. Tel.: +381 11 3370 060; fax: +381 11 324 8681.
E-mail address: gvozdic@etf.rs (D.M. Gvozdić).

0010-4655/$ – see front matter
doi:10.1016/j.cpc.2010.09.014

On the other hand, the expansion methods [18–20] are more suitable for Hamiltonians which complexity overcomes the simple elliptic interface problems. Good examples of complex Hamiltonians are those implemented in the multiband Schrödinger equation [18,20] or those which include bulk-inversion-asymmetry terms [21]. The size of the Hamiltonian matrix for the expansion methods depends on the quality and number of basis functions involved in the expansion. However, the density of Hamiltonian matrices is usually large and does not depend significantly on the Hamiltonian complexity, making the method suitable for complex Hamiltonians. Although, these Hamiltonian matrices might be of moderate size, due to their large density, they require long computational time for the diagonalization, which is usually proportional to the third power of the matrix size. In addition to that, evaluation of the Hamiltonian matrix may take a lot of computational power if it is performed by numerical integration.

The method which is generally very popular due to its simplicity, even in the case of complex Hamiltonians, and which provides a high order convergence rate and sparse discretization matrices, is the finite differences method (FDM) [22]. However, the FDM in principle requires that the heterointerfaces are flat or polygonal, since otherwise they may not be aligned with the grid, but rather crossing between the grid points, causing low approximation accuracy [23]. This limits the class of problems which can be considered by the FDM. From that point of view, the band structure analysis of nanostructures such as quantum dots and dashes might look beyond capabilities of the FDM, since their shape is rarely described by flat heterointerfaces, but rather with various lens-like curves.

It is well known that in some cases coordinate transformations may simplify geometry of the structure and computational domain, leading to the flat interfaces of the structure and computational domain, and enabling implementation of the FDM within a new coordinate space [24–26]. In the case of nanostructures where confinement is two dimensional (2D), the most efficient coordinate transformations are based on conformal mapping [19], since the kinetic part of the Hamiltonian in the mapped space has the form of the Laplacian multiplied by the determinant of the Jacobian matrix, while the mixed derivatives do not appear in the Hamiltonian. On the other hand, in some cases, the computational domain may consist of several subdomains [25], requiring more than one function to achieve flat boundaries in the mapped space. In these cases, the subdomains must be cautiously connected in order to avoid the loss of accuracy, requiring additional programming efforts. Moreover, the flat computational domain obtained after mapping, might be of inadequate size with respect to the wavefunction distribution or grid density. In other words, the equidistant grid in the mapped space may correspond to a dense grid in the region of the original space where the wavefunction changes relatively slowly, while a coarse grid may cover the region characterized by rapid change of the wavefunction, affecting in such a manner the accuracy of calculation. Similarly, it may happen that a large computational domain in the mapped space corresponds to a small domain in the original space, insufficient to accommodate the wavefunctions. However, a large computational domain in the mapped space may lead to the huge discretization matrices, which are demanding for the diagonalization or which, in spite of their size, may not provide a sufficient accuracy of the calculated eigenenergies.

In this paper, we propose a numerical method based on the combination of coordinate transformation and the FDM, which provides an efficient and simple approach for the band structure and wavefunction calculations of quantum dash nanostructures, with various cross-section shapes, widths and heights. We focus our research on the quality of the coordinate transformation with respect to simultaneous heterointerface fitting and definition of the computational domain. In other words, we search for mappings which can provide suitable computational domains, sufficient to accommodate wavefunctions, and simultaneously enabling successful fitting of the well-barrier heterointerface. A special attention is given to QDHs with the lens-like cross-section profile representing the most frequently adopted approximation for the QDH shape [4,12,27]. However, we additionally extend our approach to the case in which the QDH cross-section profile can be approximated with a trapezoidal shape [10,28,29].

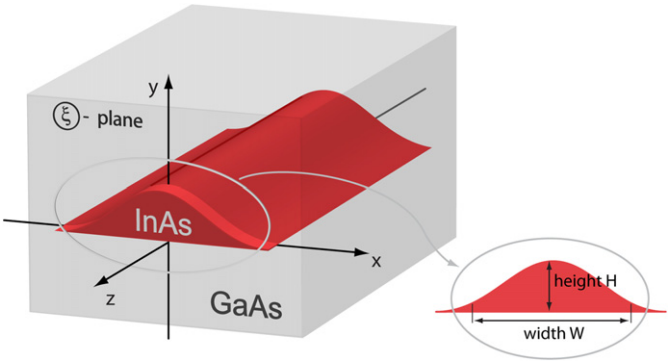

Fig. 1. (Color online.) Schematic of InAs lens-like quantum dash embedded in GaAs infinite host matrix.

In Section 2 we define geometry of the quantum dash profile and based on it, we present the theory behind the numerical method. In Section 3 we consider the most important features which have to be satisfied by the coordinate transformation and propose several possible fitting solutions for different profiles of QDH cross-sections. In Section 4, we investigate the influence of the discretization step and domain size on the convergence of the method and investigate two coordinate transformations for two different QDH profiles. Finally, in Section 5 we present our conclusions.

2. Description of the method

In order to give a detailed description of the theory behind our numerical method, we shortly discuss and analyze geometrical and compositional structure of a single QDH based on InAs well material, which is embedded in GaAs host matrix (cf. Fig. 1). The effective mass for InAs ($m^*_{\mathrm{InAs}} = 0.0221m_0$) and GaAs ($m^*_{\mathrm{GaAs}} = 0.0623m_0$), as well as the conduction band offset ($\Delta E_c = 858.7$ meV), are taken from [30], where m_0 is the free electron mass. Since QDH is an elongated InAs island [9], the well material has almost a quantum-wire nature. Therefore, the band structure of the QDH is mainly dependent on the two-dimensional (2D) carrier confinement in the transversal direction (xy plane in Fig. 1). This confinement, on the other hand, is defined by the profile of QDH cross-section. The most common geometrical approximation of the QDH's cross-section is the lens-like profile [4,12,27], which is shown in Fig. 1. The profile may slightly differ from the lens-like shape depending on the material system and growth conditions. Other common shapes used for the profile approximation are triangular [2,31,32], trapezoidal [10,28,29] and rectangular [8,33,34]. In the case of rectangular and triangular shapes, the FDM can be directly applied, without using the coordinate transformation [23]. The coordinate transformations proposed in our paper are capable to fit lens- and trapezoidal-like shapes. It should be noted that there are more sophisticated coordinate transformations, which can additionally include wetting layer into computation, but they will be considered elsewhere.

The method proposed in this paper consists of four major steps:

1. Selection of a coordinate transformation, which can provide satisfactory fit of the well-barrier heterointerface and size of the computational domain.
2. Mapping of the Hamiltonian into new coordinate space by using the Jacobian matrix for the selected coordinate transformation.
3. The Hamiltonian discretization according to the finite differences scheme and setting of the discretization matrix.
4. Evaluation of the eigenvalues representing the bound states in the QDH. This is done by using specialized routines for eigenvalue computation (LAPACK).

Before we deal with a deeper investigation of suitable coordinate transformations and their features (step 1), we give description of the Hamiltonian mapping and the FDM discretization (steps 2 and 3). We start from the EFA Schrödinger equation for electrons in the conduction band:

$$-\frac{\hbar^2}{2}\left[\frac{\partial}{\partial x}\left(\frac{1}{m^*}\frac{\partial\psi}{\partial x}\right)+\frac{\partial}{\partial y}\left(\frac{1}{m^*}\frac{\partial\psi}{\partial y}\right)\right]+\left[\frac{\hbar^2k_z^2}{2m^*}+U\right]\psi=E\psi, \tag{1}$$

where $\psi=\psi(x,y)$ is the slowly varying part of the total wavefunction, $U=U(x,y)$ is the 2D potential profile determined by the QDH's cross-section and the conduction band offset, $m^*=m^*(x,y)$ is the electronic effective mass, while E is the confinement energy, referenced to the conduction band edge of the QDH barrier material. Due to the elongated geometry of the QDH, the quantization in the longitudinal direction (z-direction) leads to a quasi-continuous subband structure, the energy of which is well approximated with parabolic dependence on corresponding wavevector (k_z). In our analysis we are interested in eigenenergies corresponding to the subband bottom, for which $k_z=0$.

By imposing the continuity of the probability density and the probability current, it is shown that $\psi(x,y)$ and its gradient perpendicular to the interface divided by the effective mass, must be continuous at the material heterointerfaces. Since we implement the finite differences scheme, the boundary conditions are naturally built in into the discretization and need not be enforced explicitly.

Once the coordinate transformation $x=x(u,v)$, $y=y(u,v)$ is chosen, where $\xi=\xi(x,y)$ represents the old coordinate space, the Schrödinger equation can be mapped into new $w=w(u,v)$ space:

$$\begin{aligned}-\frac{\hbar^2}{2}\Bigg[&u_x\frac{\partial}{\partial u}\left(\frac{u_x}{m^*}\frac{\partial\psi}{\partial u}+\frac{v_x}{m^*}\frac{\partial\psi}{\partial v}\right)+v_x\frac{\partial}{\partial v}\left(\frac{u_x}{m^*}\frac{\partial\psi}{\partial u}+\frac{v_x}{m^*}\frac{\partial\psi}{\partial v}\right)\\&+u_y\frac{\partial}{\partial u}\left(\frac{u_y}{m^*}\frac{\partial\psi}{\partial u}+\frac{v_y}{m^*}\frac{\partial\psi}{\partial v}\right)+v_y\frac{\partial}{\partial v}\left(\frac{u_y}{m^*}\frac{\partial\psi}{\partial u}+\frac{v_y}{m^*}\frac{\partial\psi}{\partial v}\right)\Bigg]\\&+U\psi=E\psi.\end{aligned} \tag{2}$$

In Eq. (2) $\psi[x(u,v),y(u,v)]=\psi(u,v)$, $U[x(u,v),y(u,v)]=U(u,v)$, while u_x, v_x, u_y, and v_y are the elements of the Jacobian matrix J_{xy} representing partial derivatives of the inverse functions $u=u(x,y)$ and $v=v(x,y)$ with respect to x and y. Since we want to set the Schrödinger equation in the w-space we need elements of J_{xy} matrix to be expressed as functions of u and v, i.e. $u_x=u_x(u,v)$, $v_x=v_x(u,v)$, $u_y=u_y(u,v)$, $v_y=v_y(u,v)$. Thus, we start from the transformation $x=x(u,v)$, $y=y(u,v)$ and its corresponding Jacobian matrix J_{uv}, which is explicit function on u and v given by:

$$J_{uv}=\begin{bmatrix}x_u & x_v\\ y_u & y_v\end{bmatrix}, \tag{3}$$

where subscripts denote the partial derivatives with respect to u and v. As the Jacobian matrix J_{xy} for the inverse mapping $u=u(x,y)$, $v=v(x,y)$ is given by $J_{xy}=J_{uv}^{-1}$, we finally derive J_{xy} as:

$$J_{xy}=\begin{bmatrix}u_x & u_y\\ v_x & v_y\end{bmatrix}=\begin{bmatrix}x_u & x_v\\ y_u & y_v\end{bmatrix}^{-1}, \tag{4}$$

which is now an explicit function on u and v.

The elements of matrix J_{xy} depend on the selected coordinate transformation. The general form of the transformation used for fitting the heterointerface and definition of the computational domain is given by:

$$x=Cu, \tag{5a}$$

$$y=Cf(u,v), \tag{5b}$$

where C is a scaling factor, expressed in nanometers. This type of coordinate transformation leads to simpler forms of the Jacobian matrices J_{uv} and J_{xy}:

$$J_{uv}=\begin{bmatrix}x_u & x_v\\ y_u & y_v\end{bmatrix}=\begin{bmatrix}C & 0\\ Cf_u & Cf_v\end{bmatrix}, \tag{6a}$$

$$J_{xy}=\begin{bmatrix}u_x & u_y\\ v_x & v_y\end{bmatrix}=\begin{bmatrix}1/C & 0\\ -f_u/(Cf_v) & 1/(Cf_v)\end{bmatrix}=\frac{1}{C}\begin{bmatrix}1 & 0\\ \mu & \rho\end{bmatrix}, \tag{6b}$$

where f_u and f_v are derivatives of $f(u,v)$ with respect to u and v, respectively, $\mu=\mu(u,v)=C\cdot v_x=-f_u/f_v$ and $\rho=\rho(u,v)=C\cdot v_y=1/f_v$. It is important to note that function $f(u,v)$ is such that the determinant of the Jacobian matrix is different than 0, i.e. $|J_{uv}|=|J_{xy}|^{-1}=C^2\cdot f_v\neq 0$. In this case, the transformation is "one to one" in the neighborhood of a point and it has the inverse transformation in all domain points. In the case of transformation given by (5), Eq. (2) is simplified and becomes:

$$\begin{aligned}-\frac{\hbar^2}{2C^2}\Bigg[&\frac{\partial}{\partial u}\left(\frac{1}{m^*}\frac{\partial\psi}{\partial u}+\frac{\mu}{m^*}\frac{\partial\psi}{\partial v}\right)+\mu\frac{\partial}{\partial v}\left(\frac{1}{m^*}\frac{\partial\psi}{\partial u}+\frac{\mu}{m^*}\frac{\partial\psi}{\partial v}\right)\\&+\rho\frac{\partial}{\partial v}\left(\frac{\rho}{m^*}\frac{\partial\psi}{\partial v}\right)\Bigg]+U\psi=E\psi.\end{aligned} \tag{7}$$

If we use standard central differences, we can discretize Eq. (7) as follows:

$$\begin{aligned}-\frac{\hbar^2}{2C^2}\Bigg\{&\frac{1}{h_u}\Bigg[\left(\frac{1}{m^*}\right)_{i+1/2,j}\frac{\psi_{i+1,j}-\psi_{i,j}}{h_u}-\left(\frac{1}{m^*}\right)_{i-1/2,j}\\&\times\frac{\psi_{i,j}-\psi_{i-1,j}}{h_u}+\left(\frac{\mu}{m^*}\right)_{i+1/2,j}\frac{\psi_{i+1/2,j+1/2}-\psi_{i+1/2,j-1/2}}{h_v}\\&-\left(\frac{\mu}{m^*}\right)_{i-1/2,j}\frac{\psi_{i-1/2,j+1/2}-\psi_{i-1/2,j-1/2}}{h_v}\Bigg]\\&+\frac{(\mu)_{i,j}}{h_v}\Bigg[\left(\frac{1}{m^*}\right)_{i,j+1/2}\frac{\psi_{i+1/2,j+1/2}-\psi_{i-1/2,j+1/2}}{h_u}\\&-\left(\frac{1}{m^*}\right)_{i,j-1/2}\frac{\psi_{i+1/2,j-1/2}-\psi_{i-1/2,j-1/2}}{h_u}\\&+\left(\frac{\mu}{m^*}\right)_{i,j+1/2}\frac{\psi_{i,j+1}-\psi_{i,j}}{h_v}-\left(\frac{\mu}{m^*}\right)_{i,j-1/2}\frac{\psi_{i,j}-\psi_{i,j-1}}{h_v}\Bigg]\\&+\frac{(\rho)_{i,j}}{h_v}\Bigg[\left(\frac{\rho}{m^*}\right)_{i,j+1/2}\frac{\psi_{i,j+1}-\psi_{i,j}}{h_v}\\&-\left(\frac{\rho}{m^*}\right)_{i,j-1/2}\frac{\psi_{i,j}-\psi_{i,j-1}}{h_v}\Bigg]\Bigg\}+U_{i,j}\psi_{i,j}=E\psi_{i,j},\end{aligned} \tag{8}$$

Table 1
A set of functions $g(u), h(v)$, and $\gamma(v)$ which satisfy conditions required for coordinate transformation, where n, m and p are positive integers.

Suggested functions for $g(u)$: $(G + B \cdot u^{2m})^{-1}$; $\exp(-B \cdot u^{2m})$; $\mathrm{sech}(B \cdot u^{m})$; $\mathrm{sech}(G + B \cdot u^{2m})$
Suggested functions for $h(v)$: v^{2n+1}; $\sinh(A \cdot v^{2n+1})$
Suggested functions for $\gamma(v)$: $(F + K \cdot v^{2p})^{-1}$; $\mathrm{sech}(K \cdot v^{p})$; $\mathrm{sech}(F + K \cdot v^{2p})$

where i and j denote indices of the discretization points, while h_u and h_v are discretization steps, along u and v coordinate, respectively. It can be seen from Eq. (8) that the implemented discretization method preserves continuity of the probability density and the probability current, since the effective masses remain under the derivative. By imposing the Dirichlet boundary conditions at the boundary of the computational domain, where the wavefunction is equal to zero, we evaluate the discretization matrix by using relation (8). It is important to note that for an accurate calculation of eigenenergies the effective mass at mid-points ($i + 1/2$ or $j + 1/2$) has to be calculated as an average of the effective masses in adjacent points, rather than the average of their reciprocal values, as one may expect by inspection of relation (8).

3. Coordinate transformation

There are several coordinate transformations which can fit the heterointerfaces of the QDH shown in Fig. 1. Thus we can consider $f(u, v)$ as a family of functions. This family is not uniquely defined, but rather has to fulfill certain conditions. Although transformations defined by the function family may lead to similar cross-section profiles, they may differ significantly depending on the fitting parameters defining function $f(u, v)$. It means that in spite of the fact that functions are not the same, for properly adopted fitting parameters, they provide same or similar cross-section profiles. Having in mind the profile of the QDH, it is obvious that in order to fit the well-barrier heterointerface, $f(u, v)$ has to be Gaussian-like with respect to u, i.e. an even function, decaying with $|u|$ and with the maximum at $u = 0$. On the other hand, for the outer dash region, i.e. the barrier, $f(u, v)$ has to provide similar profile as for the well-barrier heterointerface, which for larger $|v|$, has to be wider with respect to u, and enabling, in such a way, enclosure of the QDH structure and determination of the computational domain. This reasoning leads to possible solutions for the function $f(u, v)$, which can be represented as a product of two functions, where one depends on u and the other on v, i.e. $f(u, v) = h(v) \cdot g(u)$. In $f(u, v)$, $g(u)$ is a Gaussian-like function, while $h(v)$ is any odd function, which modulo is monotonically increasing with $|v|$. In such a manner, $h(v)$ modulates the magnitude of $g(u)$, and enables enlargement of the domain which surrounds the well material of the QDH, either for positive and negative values of v. The description of functions $h(v)$ and $g(u)$ offers several possible solutions and some of them are given in Table 1, where A, B, G, n and m are fitting parameters.

Fig. 2 shows various profiles, which can fit the QDH heterointerface, obtained as combination of the first three functions $g(u)$ and function $h(v) = \sinh(A \cdot v)$. However, the most of the proposed solutions lead to domains which size, for large u, very slowly or almost negligibly increases with $|v|$, causing rapid shrinking of the computational domain, for which $y(u, v) \approx 0$. As a matter of fact, this shrinking is suitable for the fitting of the upper QDH heterointerface, but not for the computational domain. The requirement for a relatively opened computational domain in the x-direction comes from the fact that wavefunctions may significantly "spill out" in the vicinity of the QDH corners, where the upper and

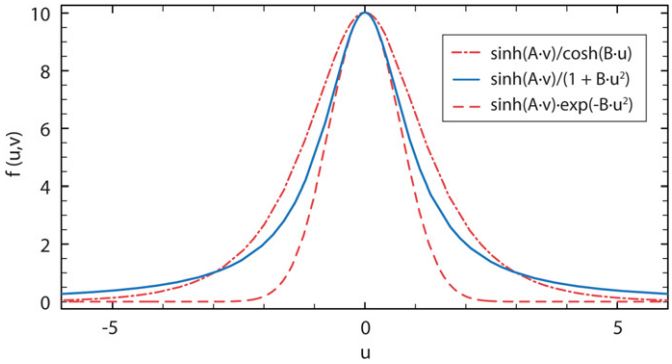

Fig. 2. (Color online.) The Gaussian-like cross-section profiles obtained for some combinations of the functions $h(v)$ and $g(u)$ given in Table 1, and for $v = 2.5$, $A = 1.2$, $B = G = 1$, $C = 1$ nm and $m = 1$.

lower heterointerface join. Thus, it is necessary to preserve suitable Gaussian-like features of the function $g(u)$ and to add a new one, which reduces decay of the function $g(u)$, preventing collapse of the computational domain for large u. This can be achieved by introducing an additional, even function $\gamma(v)$, which monotonically decays with respect to $|v|$ and modulates the argument of function $g(u)$, reducing it for larger $|v|$. Finally, we end up with the function $f(u, v) = h(v) \cdot g[\gamma(v) \cdot u^{q}]$, where q stands for $2m$ or m, while m is a positive integer. Since the function $\gamma(v)$ has the same features as the function $g(u)$ proposed in Table 1, $g(u)$ can be used as a model for the function $\gamma(v)$. According to Table 1, $\gamma(v)$ is derived from $g(u)$, after parameters G, B and m in the function $g(u)$ are replaced with F, K and p, respectively.

Starting from the previous consideration, we construct a simple coordinate transformation, which provides fit for the lens-like cross-section profile of the QDH and a reasonably small computational domain, which can accommodate the wavefunctions of the bound states:

$$x = Cu, \tag{9a}$$

$$y = \frac{C \sinh(Av)}{\cosh[Bu/\cosh(Kv)]}. \tag{9b}$$

In Fig. 3 we show how each of the parameters in coordinate transformation (9) influence the shape of the function $f(u, v)$, for a fixed value of $v = 3.5$. It can be seen that A affects the maximum of the curve, which exponentially increases with A, while B and K control the width of the Gaussian-like shape. An increase in B leads to decrease in the curve width, while the increase in K leads to its increase. Moreover, the curve shape and its width are more dependent on K than on B. Since $f(u, v)$ depends on the products $A \cdot v$ and $K \cdot v$, the previous consideration indicates that for a fixed A and K, an increase in v is equivalent to the increase in A and K for a fixed v. Thus, the increase in v simultaneously increases the maximum of the curve and its width, allowing expansion of the computational domain for large $|u|$. It means that the chosen function enables successful fitting of the upper QDH heterointerface, while for a larger $|v|$ leads to a wider curve which might represent the boundary of the computational domain.

However, the excellent fitting features of the chosen function (9) do not necessarily correlate with the function invertibility. As it is mentioned in the previous chapter, these features depend on the Jacobian determinant, which has to be different from zero at all points of the computational domain. Thus, we need to analyze the elements of the Jacobian matrix J_{uv}, especially $y_v = y_v(u, v)$, which in this case, represents the Jacobian determinant (cf. Eq. (6a)) divided by C:

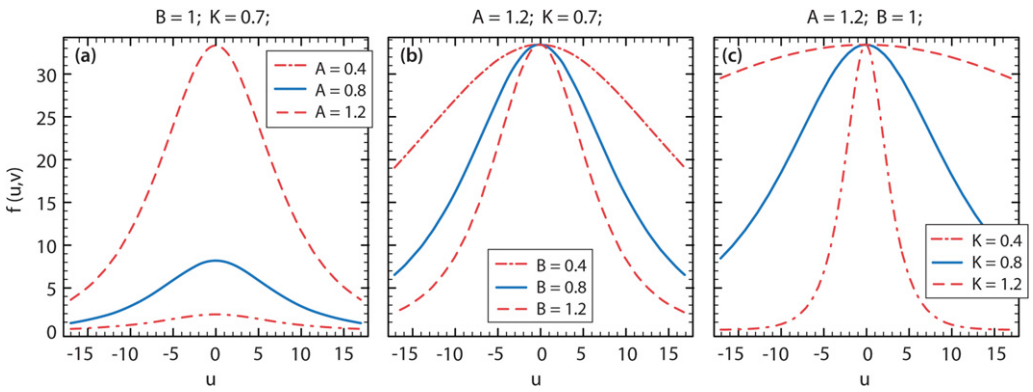

Fig. 3. (Color online.) Influence of the fitting parameters on the coordinate transformation given by relation (9).

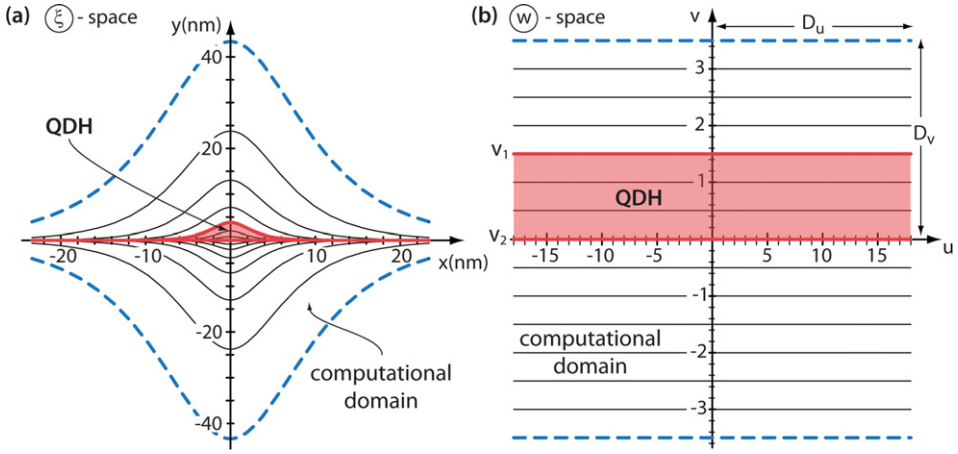

Fig. 4. (Color online.) The cross-section profile of QDH and the computational domain in the (a) ξ- and (b) w-space.

$$y_v = \frac{\partial y}{\partial v} = C\frac{A\cosh(Av) + BKu\sinh(Av)\sinh(Kv)\frac{\tanh[Bu/\cosh(Kv)]}{\cosh^2(Kv)}}{\cosh[Bu/\cosh(Kv)]}. \tag{10}$$

The functions which determine the elements in the Jacobian matrices J_{uv} and J_{xy} are given in Appendix A. Relation (10) determines $|J_{uv}|/C$, which is different from zero for any argument u and v, providing the existence of the inverse coordinate transformation and J_{xy} matrix. Although $|J_{uv}|$ has no zeros within the computational domain, the determinant decreases with $|u|$ and approaches the zero for large $|u|$ and small $|v|$ and may affect the accuracy of computation. However, this situation does not occur in the practice for common sizes of the computational domain. From the previous discussion, we conclude that the chosen transformation satisfies the most important requirements for successful implementation of the FDM including a significant domain enlargement for small variation in v.

As it is already mentioned, the profile of the QDH cross-section in some cases can be approximated with a trapezoidal shape, which can be fitted by the proper combination of the functions enlisted in Table 1. One possible solution is to use the following coordinate transformation:

$$x = Cu, \tag{11a}$$

$$y = \frac{C\sinh(Av)}{\cosh[Bu^2/(F + Kv^2)]}. \tag{11b}$$

Although this mapping leads to the trapezoidal cross-section profile, in the case of very wide structures (large $|u|$), the Jacobian determinant is too small (≈ 0) and the mapping becomes inefficient. Thus, for such structures we adopt a modified mapping, for which the argument in denominator saturates for large $|u|$. In order to fit experimentally found trapezoidal cross-section profile given in [10], we use following coordinate transformation:

$$x = Cu, \tag{12a}$$

$$y = \frac{C\sinh(Av)}{\cosh[G\tanh(Bu^q)/\cosh(Kv^p)]}, \tag{12b}$$

where p and q are positive integers. The corresponding elements of the Jacobian matrices J_{uv} and J_{xy} for the coordinate transformation given by relation (12) are given in Appendix B. The conclusions concerning the coordinate transformation features derived for the lens-like approximation are also valid in this case.

4. Computational results and discussion

In order to characterize and explore our method, we analyze the influence of the grid density and the computational domain size on the calculated eigenenergies. The first step in this analysis is to find a computational domain, for which the wavefunctions, corresponding to the eigenenergies of the QDH, can completely accommodate in the domain. The dimensions of the QDH given in Fig. 4 ($W \approx 14$ nm, $H = 3.5$ nm) are typical for InAs/GaAs material system. For this QDH structure, we find two bound states in the conduction band. As shown in Fig. 4(b), the upper heterointerface is mapped into $v_1 = 1.5$, while the lower corresponds to $v_2 = 0$. The selected domain size in the mapped space is $D_u = \pm 17$ and $D_v = \pm 3.5$, while the fitting parameters are $C = 1.3$ nm, $A = 1.2$, $B = 1$, $K = 0.7$.

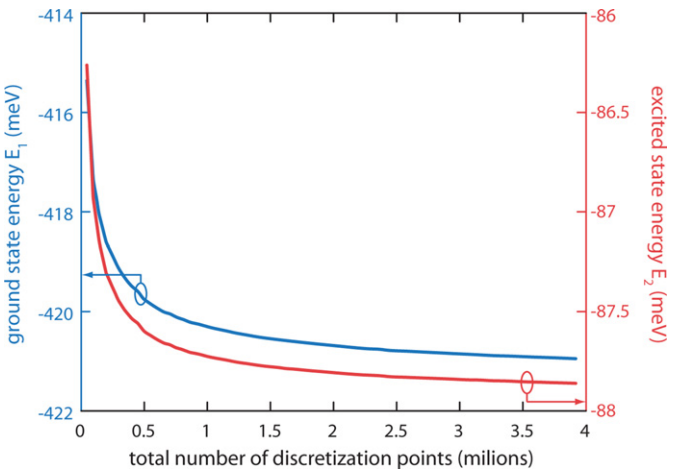

Fig. 5. (Color online.) The ground and the 1st excited state energy versus the total number of discretization points.

For the selected domain, we proportionally and gradually change the grid density in both directions and calculate eigenvalues for the QDH in Fig. 4. The discretization steps are equal in both directions, i.e. $\Delta = h_u = h_v$. Since the domain is fixed and the discretization steps are same in both directions, mutual ratio of the number of points in both directions is kept fixed. Thus, in further consideration, we do not consider the number of points in each direction (N_u, N_v), but rather the total number of grid points $(N_{uv} = N_u \times N_v)$, corresponding to the size of the discretization matrix. We use this quantity as a figure of merit for the computational time and memory resources required by the method.

Fig. 5 shows dependence of the calculated eigenenergies for both bound states versus the total number of grid points N_{uv}. It can be seen that for small number of the grid points, the eigenenergies rapidly decay and then gradually saturate with further increase in the grid density. The threshold of saturation is not clearly noticeable, although it can be seen that the difference between the eigenvalues for the largest $(\approx 4 \cdot 10^6)$ and any other grid density, becomes smaller than 1 meV, when the total number of grid points is larger than $6 \cdot 10^5$, for the ground state, and $3 \cdot 10^5$, for the

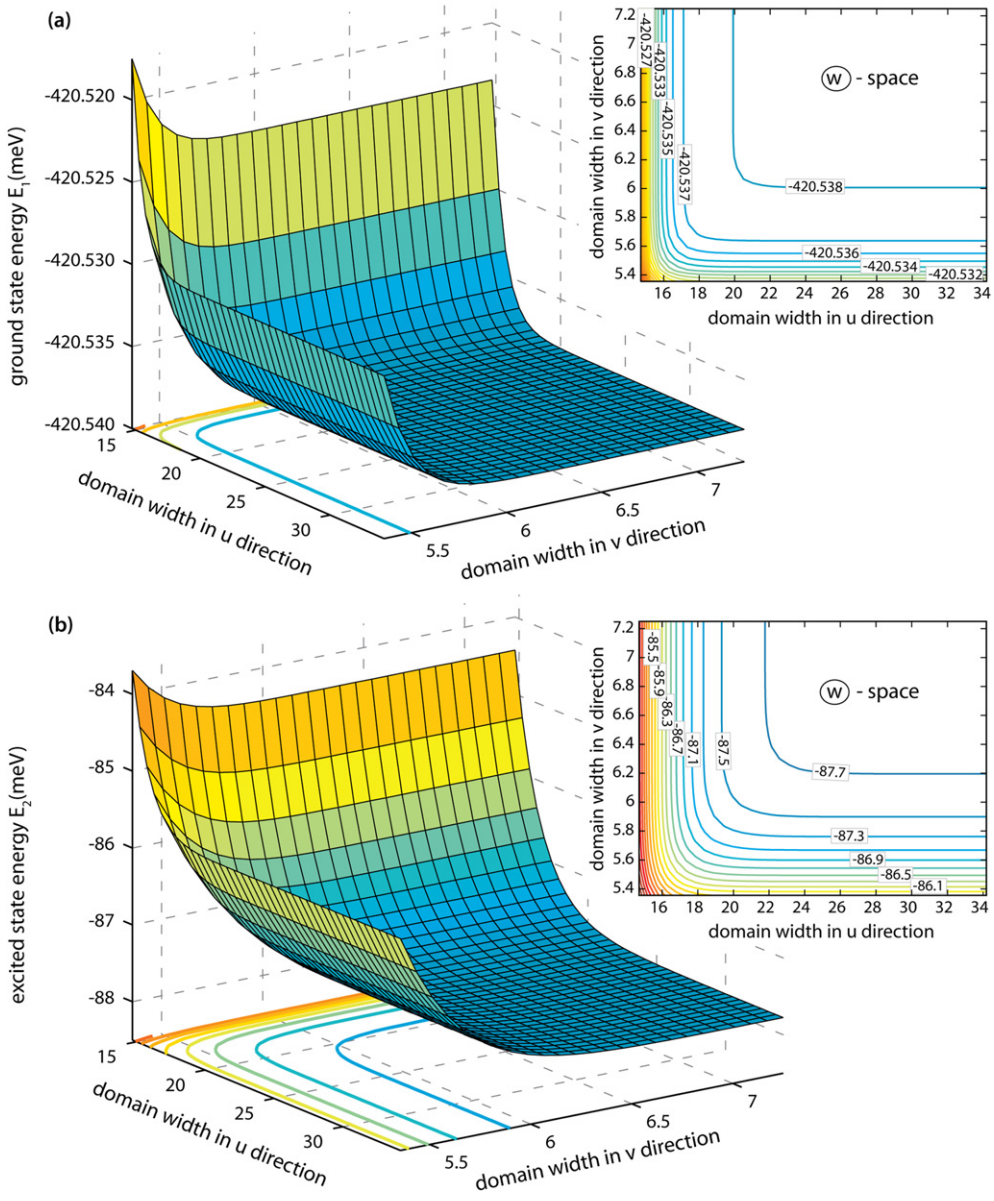

Fig. 6. (Color online.) Energy of the ground (a) and the 1st excited state (b) versus computational domain size in the w-space.

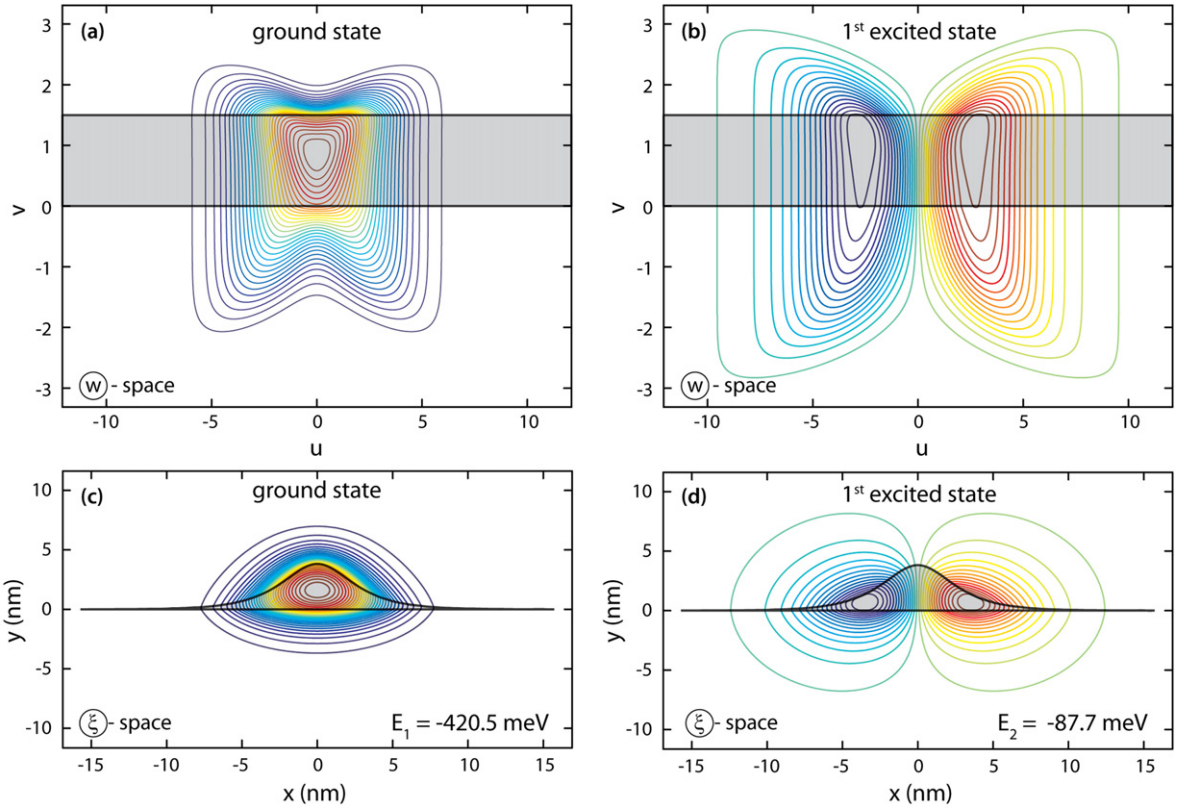

Fig. 7. (Color online.) Contour plot of the wavefunctions for the ground and 1st excited state in the ξ- and w-space for the QDH structure given in Fig. 4.

1st excited state. It means that the 1st excited state is less sensitive on the grid density than the ground state. Moreover, the total variation in the energy of the 1st excited state (from -86.3 meV to -87.8 meV) with the number of discretization points is almost four times smaller than for the ground state (from -415 meV to -421.2 meV). In order to achieve a trade-off between the accuracy and the computational time, we set a criterion for the optimal number of grid points. If the deviation of calculated eigenenergies from the eigenenergy obtained for the largest number of discretization points is smaller than 1 meV, for all eigenstates, we consider the number of discretization points sufficient and acceptable for further computation. According to Fig. 5 we find that the minimum number of total discretization points for the given computational domain and accurate calculation is $6 \cdot 10^5$. In other words, this number of points is the optimal one, for the adopted domain size and accuracy of 1 meV.

By using the dependence shown in Fig. 5, we are able to calculate the convergence rate of our method, which is ≈ 1 for the ground state and ≈ 1.3 for the first excited state [25]. This is an expected result, having in mind that the standard version of the finite differences has been implemented. However, the convergence rate can be improved by implementation of more sophisticated discretization methods, which we do not study here.

In order to make a fair comparison with the FEM, we perform the FEM calculation on the computational domain in ξ-space, which fully corresponds to domain used by our method in w-space. At the same time, we keep the number of elements in the FEM computation approximately equal to the number of points N_{uv}. However, a direct correspondence between number of points in our methods and elements in the FEM is not fully justified since the mesh in the FEM is not homogeneous as in the FDM. We find a fairly good agreement with our calculation, for which the eigenenergies differ less than one tenth of 1 meV from the eigenenergies calculated by the FEM. Regarding the computational time, we find our method more favorable than the FEM. As an illustration, we present the test of two methods performed on a desktop computer using 64-bit Windows 7 platform with Intel Core2Quad@2.66 GHz processor and 8 GB DDR2 memory (available physical memory 6.47 GB). After setting the number of discretization points (or FEM elements) to $N_{uv} = 0.55$, 1.27, 1.87 millions, our method completes calculation in 2.3, 13, and 34.1 min, while the FEM runs for 15.5, 82.3, and 179.6 min, respectively. This indicates that our method is at least 5 times faster than the FEM. Although our method is still superior for larger number of points, the comparison is not further reliable since both methods start to use virtual memory.

In Fig. 6 we show the energies of the ground and the first excited state versus the domain size in the u and v direction, for a fixed discretization step $\Delta = 0.013$. As one may expect, if the domain size is too small either in the u or v direction, the wavefunction cannot accommodate properly in the computational domain. In this case, a narrow domain acts as an additional infinite potential, raising the eigenenergies of both bound states. The domain for which the energy of the excited state reaches the saturation is not easy to recognize, although one can roughly adopt the region $2D_u \geqslant 20$ and $2D_v \geqslant 5.8$, for which variation in the eigenenergy is smaller than 0.5 meV. The situation is much more favorable for the ground state, which is less sensitive on variations in the domain size. In this case, the order of magnitude of the ground state energy variation is 10^{-2} meV for all considered dimensions of the computational domain, which is almost negligible in comparison with the first excited state. It can be seen that the saturation region is much more pronounced than for the excited state and comprises region $2D_u \geqslant 18$ and $2D_v \geqslant 5.7$, in which the energy variation is smaller than 10^{-3} meV. It should be noted that the sufficient domain size in w-space does not depend on actual QDH size but rather on its shape i.e. its width and height ratio. This feature is enabled by scaling factor C, which is used to set all

dashes of the same shape, regardless to their size, into the same domain in w-space.

In Fig. 7 we show the distribution of the wavefunction in the $\xi = \xi(x, y)$ and $w = w(u, v)$ space. It can be seen that in the w-space the wavefunctions for both states (Fig. 7(a)) are compressed along the v-direction in the middle of the computational domain. This is a consequence of implemented mapping, which in the w-space expands the region in the vicinity of the QDH corners and simultaneously compresses the space in the middle of the QDH. After implementation of the inverse mapping from the w- to the ξ-space, both wavefunctions nicely fit in the chosen computational domain.

In the case of trapezoidal QDH given in Ref. [10], we use the coordinate transformation (12) and find following fitting parameters: $p = 2$, $q = 6$, $A = 1$, $C = 1.5$ nm, $G = 20$, $B = 10^{-5}$, and $K = 1$. The corresponding fit of the QDH cross-section profile and the computational domain in the ξ-space are shown in Fig. 8. The form of the computational domain in the mapped space is the same as in Fig. 4(b). It should be noted that the mapping given by relations (11), although simpler, can reproduce narrower and higher trapezoidal shapes.

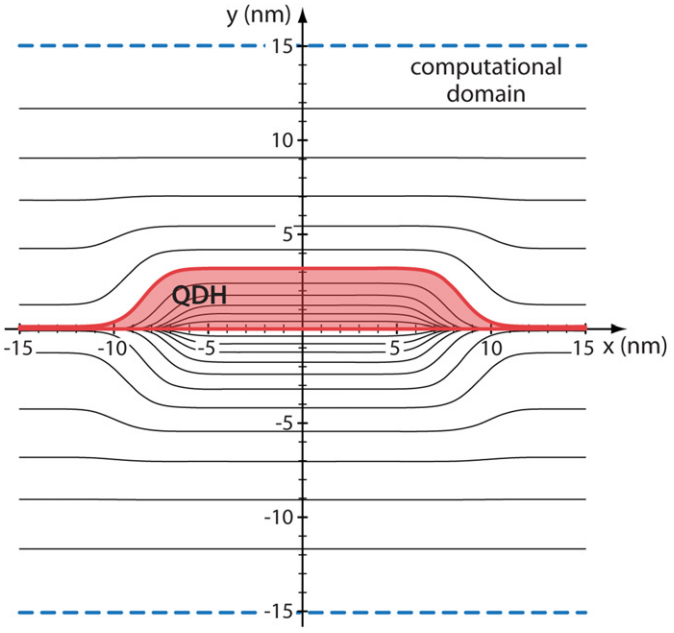

Fig. 8. (Color online.) The trapezoidal QDH profile and corresponding computational domain.

By implementing the same procedure as before, we calculate the corresponding discrete energies and wavefunctions shown in Fig. 9, which nicely accommodate into the selected computational domain. However, the problem in this case is the elongated shape of the QDH profile, which in comparison with the height of the QDH is one order of the magnitude larger and thus very difficult to fit with a simple combination of functions. Relation (12) provides not only a very broad and flat upper heterointerface of the QDH, but also the proper angle of the lateral sides of the trapeze. This angle is very important since it significantly affects the wavefunction distribution and indicates that approximation of the QDH by simple rectangular shape is not an adequate replacement for the trapezoidal profile. Moreover, the proposed coordinate transformation and the method simplify the implementation of the FDM, compared to the case when the problem is solved in the original ξ-space.

5. Conclusion

The paper presents an efficient and simple method for the band structure and wavefunction calculation of quantum dashes. The method is based on the coordinate transformation of the QDH structure, the computational domain and the Hamiltonian, followed by implementation of the FDM in the new computational space. The method versatility comes from a broad set of function families which can fit the upper QDH heterointerface and generate the computational domain of the proper form and size. Some of these functions are proposed in the paper and their features are studied. We find that the coordinate transformation (9) provides simple and flexible fitting of the most common, lens-like QDH profile, while the transformation (12) is very suitable for trapezoidal QDH cross-section shape. Our numerical investigation showed that there is a sufficient computational domain size, for which the variation of the eigenenergies with domain size can be reduced below a certain limit, in our case 10^{-2} meV. For the considered lens-like profile, the sufficient domain size is $2D_u \geqslant 20$ and $2D_v \geqslant 5.8$. The limits of the sufficient domain, and consequently the total

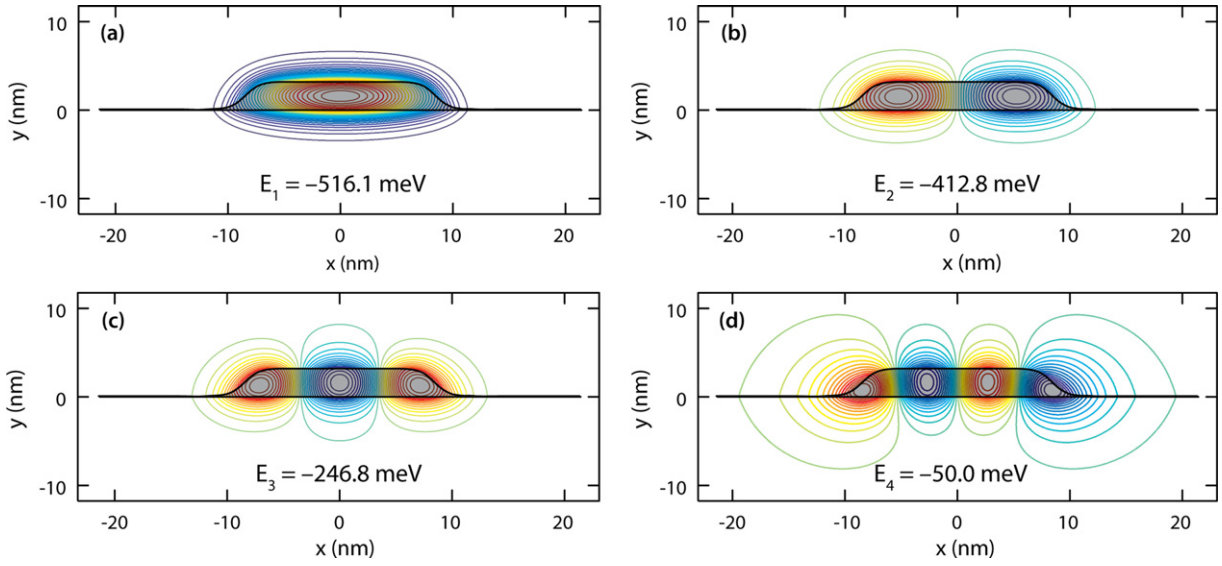

Fig. 9. (Color online.) Contour plot of the wavefunctions for the ground (a) and the first three excited states (b–d) in the ξ-space for the trapezoidal QDH structure in Fig. 8.

number of discretization points, do not depend on QDH size, but rather on their shape and dimensions ratio. Thus, the domain is the universal domain for QDHs with same shape and different sizes. For given QDH lens-like profile and the optimal total number of points (approximately $6 \cdot 10^5$) or even larger, the method provides stable eigenvalue solutions. The proposed method exhibits solid stability and flexibility with respect to the size and shape of the QDH and the computational domain. Due to its simplicity, it is very promising for implementation in the case of multiband Schrödinger-equation.

Acknowledgement

This work is supported by the Serbian Ministry of Science under project No. 160001.

Appendix A. The elements in the Jacobian matrices J_{uv} and J_{xy} for QDHs with the lens-like cross-section profile

For the coordinate transformation given by Eq. (9), the elements of the Jacobian matrix J_{uv} are:

$$y_u = \frac{\partial y}{\partial u} = -C\frac{B\sinh(Av)\sinh\left[\frac{Bu}{\cosh(Kv)}\right]}{\cosh(Kv)\cosh^2\left[\frac{Bu}{\cosh(Kv)}\right]}, \tag{A.1}$$

$$y_v = \frac{\partial y}{\partial v} = C\frac{A\cosh(Av) + BKu\sinh(Av)\frac{\sinh(Kv)}{\cosh^2(Kv)}\tanh\left[\frac{Bu}{\cosh(Kv)}\right]}{\cosh\left[\frac{Bu}{\cosh(Kv)}\right]}, \tag{A.2}$$

while, the elements of Jacobian matrix J_{xy} are:

$$v_x = \frac{\partial v}{\partial x} = \frac{1}{C}\frac{B\frac{\sinh(Av)}{\cosh(Kv)}\tanh\left[\frac{Bu}{\cosh(Kv)}\right]}{A\cosh(Av) + BKu\sinh(Av)\frac{\sinh(Kv)}{\cosh^2(Kv)}\tanh\left[\frac{Bu}{\cosh(Kv)}\right]}, \tag{A.3}$$

$$v_y = \frac{\partial v}{\partial y} = \frac{1}{C}\frac{\cosh\left[\frac{Bu}{\cosh(Kv)}\right]}{A\cosh(Av) + BKu\sinh(Av)\cdot\frac{\sinh(Kv)}{\cosh^2(Kv)}\tanh\left[\frac{Bu}{\cosh(Kv)}\right]}. \tag{A.4}$$

Appendix B. The elements in the Jacobian matrices J_{uv} and J_{xy} for QDHs with the trapezoidal cross-section profile

For the coordinate transformation given by Eq. (12), the elements of the Jacobian matrix J_{uv} are:

$$y_u = \frac{\partial y}{\partial u} = \frac{-CBGqu^{q-1}\sinh(Av)\tanh\left[G\frac{\tanh(Bu^q)}{\cosh(Kv^p)}\right]}{\cosh^2(Bu^q)\cosh(Kv^p)\cosh\left[G\frac{\tanh(Bu^q)}{\cosh(Kv^p)}\right]}, \tag{B.1}$$

$$y_v = \frac{\partial y}{\partial v} = C\Bigg(A\cosh(Av) + KGpv^{p-1}\sinh(Av) \times \tanh(Bu^q)\frac{\tanh(Kv^p)}{\cosh(Kv^p)}\tanh\left[G\frac{\tanh(Bu^q)}{\cosh(Kv^p)}\right]\Bigg) \times \left(\cosh\left[G\frac{\tanh(Bu^q)}{\cosh(Kv^p)}\right]\right)^{-1}, \tag{B.2}$$

while the elements of the Jacobian matrix J_{xy} are:

$$v_x = \frac{\partial v}{\partial x} = \frac{BGqu^{q-1}\sinh(Av)\tanh\left[G\frac{\tanh(Bu^q)}{\cosh(Kv^p)}\right]}{C\cosh^2(Bu^q)\cosh(Kv^p)} \times \Bigg\{A\cosh(Av) + GKpv^{p-1}\sinh(Av) \times \tanh(Bu^q)\frac{\tanh(Kv^p)}{\cosh(Kv^p)}\tanh\left[G\frac{\tanh(Bu^q)}{\cosh(Kv^p)}\right]\Bigg\}^{-1}, \tag{B.3}$$

$$v_y = \frac{\partial v}{\partial y} = \left(\frac{1}{C}\cosh\left[G\frac{\tanh(Bu^q)}{\cosh(Kv^p)}\right]\right) \times \Bigg(A\cosh(Av) + GKpv^{p-1}\sinh(Av) \times \tanh(Bu^q)\frac{\tanh(Kv^p)}{\cosh(Kv^p)}\tanh\left[G\frac{\tanh(Bu^q)}{\cosh(Kv^p)}\right]\Bigg)^{-1}. \tag{B.4}$$

References

[1] P. Bhattacharya, Z. Mi, Quantum-dot optoelectronic devices, Proc. IEEE 95 (2007) 1723–1740.
[2] J.P. Reithmaier, G. Eisenstein, A. Forchel, InAs/InP quantum-dash lasers and amplifiers, Proc. IEEE 95 (2007) 1779–1790.
[3] F. Lelarge, B. Dagens, J. Renaudier, R. Brenot, A. Accard, F. van Dijk, D. Make, O. Le Gouezigou, J.-G. Provost, F. Poingt, J. Landreau, O. Drisse, E. Derouin, B. Rousseau, F. Pommereau, G.-H. Duan, Recent advances on InAs/InP quantum dash based semiconductor lasers and optical amplifiers operating at 1.55 μm, IEEE J. Sel. Top. Quantum Electron. 13 (2007) 111–124.
[4] J.P. Reithmaier, A. Somers, S. Deubert, R. Schwertberger, W. Kaiser, A. Forchel, M. Calligaro, P. Resneau, O. Parillaud, S. Bansropun, M. Krakowski, R. Alizon, D. Hadass, A. Bilenca, H. Dery, V. Mikhelashvili, G. Eisenstein, M. Gioannini, I. Montrosset, T.W. Berg, M. van der Poel, J. Mørk, B. Tromborg, InP based lasers and optical amplifiers with wire-/dot-like active regions, J. Phys. D: Appl. Phys. 38 (2005) 2088–2102.
[5] A.J. Zilkie, J. Meier, M. Mojahedi, P.J. Poole, P. Barrios, D. Poitras, T.J. Rotter, C. Yang, A. Stintz, K.J. Malloy, P.W.E. Smith, J.S. Aitchison, Carrier dynamics of quantum-dot, quantum-dash, and quantum-well semiconductor optical amplifiers operating at 1.55 μm, IEEE J. Quantum Electron. 43 (2007) 982–991.
[6] A. Stintz, G.T. Liu, H. Li, L.F. Lester, K.J. Malloy, Low-threshold current density 1.3-μm InAs quantum-dot lasers with the dots-in-a-well (DWELL) structure, IEEE Photon. Technol. Lett. 12 (2000) 591–593.
[7] H. Saito, K. Nishi, A. Kamei, S. Sugou, Low chirp observed in directly modulated quantum dot lasers, IEEE Photon. Technol. Lett. 12 (2000) 1298–1300.
[8] J.H. Wei, K.S. Chan, A theoretical analysis of quantum dash structures, J. Appl. Phys. 97 (2005) 123524–123539.
[9] H. Dery, E. Benisty, A. Epstein, R. Alizon, V. Mikhelashvili, G. Eisenstein, R. Schwertberger, D. Gold, J.P. Reithmaier, A. Forchel, On the nature of quantum dash structures, J. Appl. Phys. 95 (2004) 6103–6111.
[10] H.S. Djie, C.L. Tan, B.S. Ooi, J.C.M. Hwang, X.-M. Fang, Y. Wu, J.M. Fastenau, W.K. Liu, G.T. Dang, W.H. Chang, Ultrabroad stimulated emission from quantum-dash laser, Appl. Phys. Lett. 91 (2007) 111116–111119.
[11] J.V. Crnjanski, D.M. Gvozdić, Intersubband absorption in quantum dash nanostructures, Acta Phys. Pol. A 116 (2009) 668–671.
[12] M. Gioannini, Analysis of the optical gain characteristics of semiconductor quantum-dash materials including the band structure modifications due to the wetting layer, IEEE J. Quantum Electron. 42 (2006) 331–340.
[13] T. Yamauchi, T. Takahashi, Y. Arakawa, Tight binding analysis for quantum-wire lasers and quantum-wire infrared detectors, IEEE J. Quantum Electron. 27 (1991) 1817–1823.
[14] S. Pescetelli, A.D. Carlo, P. Lugli, Conduction-band mixing in T and V-shaped quantum wires, Phys. Rev. B 56 (1997) R1668–R1671.
[15] F. Vouilloz, D.Y. Oberli, M.-A. Dupertuis, A. Gustafsson, F. Reinhardt, E. Kapon, Effect of lateral confinement on valence-band mixing and polarization anisotropy in quantum wires, Phys. Rev. B 57 (1998) 12378–12387.
[16] J.C. Yi, N. Dagli, Finite-element analysis of valence band structure and optical properties of quantum-wire arrays on vicinal substrates, IEEE J. Quantum Electron. 31 (1995) 208–218.
[17] M. Ogawa, T. Kunimasa, T. Ito, T. Miyoshi, Finite-element analysis of quantum wires with arbitrary cross sections, J. Appl. Phys. 84 (1998) 3242–3249.
[18] D.M. Gvozdić, N.M. Nenadović, A. Schlachetzki, Gain and threshold-current calculation of V-groove quantum-wire InGaAs–InP laser, IEEE J. Quantum Electron. 38 (2002) 1565–1579.
[19] D.M. Gvozdić, A. Schlachetzki, Electronic states in the conduction band of V-groove quantum wires, J. Appl. Phys. 92 (2002) 2023–2034.

[20] G. Goldoni, F. Rossi, E. Molinari, A. Fasolino, Band structure and optical anisotropy in V-shaped and T-shaped semiconductor quantum wires, Phys. Rev. B 55 (1997) 7110–7123.
[21] U. Ekenberg, D.M. Gvozdić, Analysis of electric-field-induced spin splitting in wide modulation-doped quantum wells, Phys. Rev. B 78 (2008) 205317–205326.
[22] C. Pryor, Electronic structure and optical properties of serpentine superlattice quantum-wire arrays, Phys. Rev. B 44 (1991) 12912–12917.
[23] T.-M. Hwang, W.-W. Lin, W.-C. Wang, W. Wang, Numerical simulation of three dimensional pyramid quantum dot, J. Comput. Phys. 196 (2004) 208–232.
[24] C.J. Fall, M.-A. Dupertuis, E. Kapon, Electronic states in hyperbolic-boundary crescent-shaped quantum wires, Opt. Quantum Electron. 31 (1999) 201–213.
[25] T.-M. Hwang, W.-C. Wang, W. Wang, Numerical schemes for three-dimensional irregular shape quantum dots over curvilinear coordinate systems, J. Comput. Phys. 226 (2007) 754–773.
[26] G. Creci, G. Weber, Electron and hole states in V-groove quantum wires: an effective potential calculation, Semicond. Sci. Technol. 14 (1999) 690–694.
[27] W. Rudno-Rudziński, G. Sęk, K. Ryczko, R. Kudrawiec, J. Misiewicz, A. Somers, R. Schwertberger, J.P. Reithmaier, A. Forchel, Optically probed wetting layer in InAs/InGaAlAs/InP quantum-dash structures, Appl. Phys. Lett. 86 (2005) 101904–101906.
[28] B.S. Ooi, H.S. Dije, Y. Wang, C.-L. Tan, J.C.M. Hwang, X.-M. Fang, J.M. Fastenau, A.W.K. Liu, G.T. Dang, W.H. Chang, Quantum dashes on InP supstrate for broadband emitter applications, IEEE J. Sel. Top. Quantum Electron. 14 (2008) 1230–1238.
[29] P. Miska, J. Even, C. Platz, B. Salem, T. Benyattou, C. Bru-Chevalier, G. Guillot, G. Bremond, Kh. Moumanis, F.H. Julien, O. Marty, C. Monat, M. Gendry, Experimental and theoretical investigation of carrier confinement in InAs quantum dashes grown on InP(001), J. Appl. Phys. 95 (2004) 1074–1080.
[30] I. Vurgaftman, J.R. Meyer, L.R. Ram-Mohan, Band parameters for III–V compound semiconductors and their alloys, J. Appl. Phys. 89 (2001) 5815–5875.
[31] S.P. Guo, H. Ohno, A. Shen, F. Matsukura, Y. Ohno, InAs self-organised quantum dashes grown on GaAs (211)B, Appl. Phys. Lett. 70 (1997) 2738–2740.
[32] A. Sauerwald, T. Kümmell, G. Bacher, A. Somers, R. Schwertberger, J.P. Reithmaier, A. Forchel, Size control of InAs quantum dashes, Appl. Phys. Lett. 86 (2005) 253112–253114.
[33] S.C. Heck, S.B. Healy, S. Osborne, E.P. O'Reilly, F. Lelarge, F. Poingt, A. Accard, F. Pommereau, O. Le Gouezigou, B. Dagens, An analysis of 1.55 μm InAs/InP quantum dash lasers, Appl. Phys. Lett. 92 (2008) 251105–251107.
[34] Z. Mi, P. Bhattacharya, DC and dynamic characteristics of P-doped and tunnel injection 1.65-μm InAs quantum-dash lasers grown on InP (001), IEEE J. Quantum Electron. 42 (2006) 1224–1232.